Computers, Materials &
Continua

Tech Science Press

https://doi.org/10.32604/cmc.2026.081382

ARTICLE

Halide-Driven Bandgap Engineering and SLME-Based Photovoltaic Performance of Ba_3PX_3 Compounds: A First-Principles Study

Peeyush Kumar Kamlesh[1,*], **Himanshi Sharma**[2], **Shrikant Verma**[1], **Ajay Singh Verma**[3,4],
Reena Saxena[5] **and Dinesh C. Sharma**[6]

[1]Department of Physics, Poornima University, Jaipur, Rajasthan, India
[2]School of Basic & Applied Sciences, Nirwan University Jaipur, Jaipur, Rajasthan, India
[3]Department of Allied Sciences, Graphic Era Deemed to be University, Dehradun, Uttarakhand, India
[4]Department of Physics, University Centre for Research & Development, Chandigarh University, Mohali, Punjab, India
[5]School of Applied Sciences, Suresh Gyan Vihar University, Jaipur, Rajasthan, India
[6]Department of Physics, Mahatma Jyoti Rao Phoole University, Jaipur, Rajasthan, India

*Corresponding Author: Peeyush Kumar Kamlesh. Email: peeyush.physik@gmail.com

Received: 01 March 2026; Accepted: 28 April 2026; Published: 15 June 2026

ABSTRACT: In the present work, Ba_3PX_3 (X = F, Cl, Br, I) all-inorganic and lead-free halide compositions have been studied as possible replacements for hybrid perovskites using first-principles calculations. All the considered materials were found to exhibit direct band gaps at the Γ-point, decreasing from 2.37 eV (Ba_3PF_3) to 1.48 eV (Ba_3PI_3). The optical calculations reveal strong absorption in the visible and near-UV regions, with the static dielectric constants ranging from 2.75 to 4.35 in the halide series. All the compounds are mechanically stable and have tuneable ductility and stiffness properties. Lattice stability is confirmed by thermodynamic analysis in broad temperature ranges (0–900 K) and pressure ranges (0–10 GPa). The spectroscopic limit maximum efficiency (SLME), which is a theoretical screening parameter that represents an upper limit, has a value of 39.17% at 300 K for an absorber thickness of 1 μm, comparable to practical thin-film photovoltaic architectures. The findings identify strong trends in the stability of structures, optoelectronic properties, and photovoltaic characteristics within the Ba_3PX_3 family and rank Ba_3PBr_3 and Ba_3PI_3 among the most promising lead-free photovoltaic absorbers.

KEYWORDS: Bandgap engineering; optical and dielectric response; elastic and thermodynamic stability; spectroscopic limited maximum efficiency; high-efficiency solar absorbers

1 Introduction

As the world population continues to increase steadily and industrialization progresses, energy requirements are increasing at a high rate. The conventional sources of energy are limited in nature. In addition, their rate of formation is much lower than their consumption rate. Therefore, to address the rising energy demands sustainably, there is a need to use renewable energy sources. One of the pressing challenges is the growing demand for sophisticated photovoltaic (PV) cells, optoelectronic devices, and electronic gadgets, especially with the rising energy deficits induced by population explosion [1–3]. Hybrid (organic-inorganic) perovskite solar cells (PSCs) have received a significant amount of attention in both the device fabrication and performance optimization owing to their high charge carrier mobility, low density of traps, low exciton binding energy, good optical absorption, and long carrier lifetimes [4–6].

Copyright © 2026 The Authors. Published by Tech Science Press. This work is licensed under a Creative Commons Attribution 4.0 International License, which permits unrestricted use, distribution, and reproduction in any medium, provided the original work is properly cited.

Nevertheless, to achieve environmentally sustainable PSCs, it is imperative to create compositions that are both non-toxic and environmentally friendly. Lead-free perovskites are among them, and they have gained increased attention owing to their environmental safety and potential applications in the solar and thermoelectric fields [7–10]. Currently, one of the most frequent issues in the field of perovskite solar cells (PSC) is reproducibility, as the performance of the device is usually different when the materials are changed or applied, or when different methods of fabrication are used [11,12]. In addition, mass-scale production is a major challenge, especially in the quest to achieve perovskite solar panels that are economical, high-performing, and competent in producing a substantial amount of power. Despite being characterized by excellent light absorption, long charge-carrier lifetimes, high mobility, low trap densities, and reduced exciton binding energies, hybrid PSCs are very vulnerable in terms of volatility and thermal stability; hence, they cannot be widely commercialized with organic cations [13–15].

All-inorganic, lead-free halide perovskites have received growing interest because they reduce the toxicity concerns of Pb-based hybrid perovskites and do not suffer from the thermal or moisture instability of organic cations. A_3BX_3-type compounds, in which A is an alkaline earth metal, B is a pnictogen (including P, As, or Sb), and X is a halide (including F, Cl, Br, or I), have also become options in this regard [16]. The Ba_3PX_3 (X = F, Cl, Br, and I) family of compounds has received specific interest because they are structurally stable, chemically non-toxic, and can be easily tuned in terms of their electronic and optical properties.

First-principles DFT was applied by Haque et al. [17] to demonstrate that the direct band gaps of Ba_3SbX_3 (X = F, Cl) compounds under ambient atmospheric pressure (0.9 eV) are tremendous and decline sharply under hydrostatic pressure (to 0.04–0.05 eV); however, mechanical stability is not compromised, and the optical response is enhanced, which demonstrates their great promise in pressure-tuneable optoelectronic devices. In the last few years, solar cells based on perovskite have recorded impressive gains in power conversion efficiency (PCE), rising from 2.9% to above 26.7% [18]. Moreover, it has been demonstrated that the incorporation of host lattices can improve the crystal structure and photovoltaic performance by introducing multiple electron transport layers [19–21].

It is due to the large ionic radius of Ba^{2+}, which promotes structural stability and enables substitution for halide ions, leading to modulation of the band gap, which is required for further conversion of solar energy and for photonic applications. Early first-principles density functional theory (DFT) analyses indicate that Ba_3PX_3 compounds have semiconducting band gaps, strong mechanical strength, and distinctive optical absorption features, especially in the visible and near-ultraviolet regions [22]. The impact of Cu-based Back Surface Field (BSF) layers on the performance of PSCs made of Ba_3PCl_3 is examined, as well as methods to improve their efficiency. BSF, which is CuSnSe (Copper Tin Selenide), is a good converter of power with a maximum theoretical power conversion efficiency of 31.18%. Moreover, earlier findings [23] indicate that Ba_3MX_3 (M = P, Sb; X = F, Cl) compounds have a direct bandgap, are strong optical absorbers, and are high photoconductors. The compounds were observed as mechanically stable according to the Born criteria and thermally stable over a broad temperature range, which predicts their use in photovoltaic and optoelectronic applications. Several first-principles and device-oriented investigations have recently been conducted on Ba_3PX_3-based perovskites, focusing on selective compositions, electronic bandgap properties, and optimizing performance by utilizing transport-layer and back-surface-field engineering. For example, earlier studies have reported band structures, optical absorption spectra, and device-level efficiencies for individual Ba_3PX_3 compounds, especially Ba_3PCl_3 and Ba_3PI_3, under a variety of photovoltaic conditions.

Nevertheless, these studies fail to systematically determine how the replacement of halides throughout the entire Ba_3PX_3 (X = F, Cl, Br, I) series controls the intrinsic changes in structural stability, elastic response, thermodynamic behavior, optical properties, and spectroscopically limited photovoltaic efficiency within a single computational framework. Furthermore, photovoltaic screening quantities, even realistic ones, such as the thickness- and temperature-dependent SLME proportional to first-principles optical spectra, have not consistently been linked with mechanical and thermodynamic stability tendencies. Here, the current study offers a property-level (consolidated) study of Ba_3PX_3 compounds and explicitly shows the correlation between halide chemistry and structure-property-performance correlation, which incorporates the design of lead-free photovoltaic absorbers.

2 Computational Details

This study investigated the structural, electronic, and optical behaviour of Ba_3PX_3 (X = F, Cl, Br, I) family of halide compositions through "Full-Potential Linearized Augmented Plane Wave + local orbitals" (FP-LAPW + lo) technique using the WIEN2k simulation code [24]. Geometry optimization and ground-state characteristics were evaluated within the framework of the Perdew-Burke-Ernzerhof Generalized Gradient Approximation (PBE-GGA) [25] functional. For each atom, the muffin-tin radii (R_{MT}) were chosen based on the corresponding atomic radius, where the plane-wave cutoff parameter was determined as $R_{MT} \times K_{max} = 7.5$. Structural optimization and electronic characteristics calculations were executed by employing a Monkhorst-Pack k-point mesh of 10 × 10 × 10. In order to confirm that the results are reliable, convergence tests were conducted with respect to k-point sampling and basis set size. It was found that for k-point sampling, increasing to greater than a 10 × 10 × 10 k-point mesh showed very little additional variation in total energy (<1 meV/atom) and the band gap (<0.01 eV). The maximum value of the angular momentum expansion inside the atomic spheres was taken up to $l_{max} = 10$, the maximum modulus for reciprocal lattice vectors was set to $G_{max} = 12$ a.u.$^{-1}$, and a cutoff energy of −6.0 eV was applied to separate the core and valence states. Self-consistent field (SCF) iterations were continued until the total energy satisfied a convergence criterion of 0.0001 Ry and the charge density satisfied 0.001 e. Structural relaxations were performed to obtain equilibrium lattice parameters associated with the minimum total energy of each halide compound. After optimising structures, they were further used to compute the electronic band structures, total and partial density of states (DOS), and optical characteristics. For an accurate band gap determination, the Tran-Blaha modified Becke-Johnson (TB-mBJ) [26] potential was used along with PBE-GGA. TB-mBJ produced band gaps that are similar to experimental and hybrid functional (like HSE06) calculations in many semiconductors [27,28]. While hybrid functionals have been shown to produce more accurate results but their high computational cost makes them less suitable for performing multi-property investigations. Therefore, TB-mBJ provides a method that is both accurate and efficient for characterizing the electronic characteristics of the systems evaluated in the present investigations. For computing the optical properties, a denser 20 × 20 × 20 k-point grid was adopted to capture the fine features in the spectra. Test calculations confirmed that increasing the value of k-point would result in very little difference in any optical spectrum calculation. Lattice parameter variations may affect the absolute density of k-points slightly, but using a uniform k-point grid for all compositions will provide an accurate comparison of optical trends. The ELAST package was used for evaluating elastic constants within the WIEN2k simulation code. The thermodynamic properties were calculated by utilising the Gibbs2 [29] program, evaluating at temperatures from 0 to 900 K and pressures from 0 to 10 GPa. The SLME code [30] was used to calculate the efficiency of the solar cells for varying thicknesses of each layer. The spin-orbit coupling (SOC) effects were not involved in the present study because the focus of this study is on comparative halide-dependent trends, which are not expected to be qualitatively altered by SOC. However, SOC may influence absolute band-gap values, particularly for the iodide compound, although the comparative trends across the series remain unaffected. Similar approaches have been adopted in previous first-principles studies of halide perovskites where trend analysis is the primary objective [31,32]. Spin polarized calculations were conducted for each of the compositions to determine the magnetic ground state of the different structural geometries and the calculations all converged to a non-magnetic solution with little to no spin splitting, indicating that there is no intrinsic magnetism due to the closed shell electronic configurations of the cation Ba^{2+}, the anion phosphide P^{3-}, and the halogen ions. Therefore, subsequent analysis used non-spin polarized calculations. Where possible, the calculated structural, electronic and mechanical parameters are compared to already reported theoretical and experimental values to assess the accuracy and reliability of the current method of calculation.

3 Results and Discussion

3.1 Structural Properties

Ba_3PX_3 are metal halide compositions that crystallize in the cubic Pm-3m space group. Each formula unit contains three Ba atoms, one P atom, and three halide atoms X (F, Cl, Br, or I). Ba^{2+} cations occupy the 3c Wyckoff sites (0.5, 0, 0) near the cube corners, P^{3-} anions sit at the 1a Wyckoff site (0, 0, 0) at the center of the cube, and halide X^- anions reside at the 3d Wyckoff sites (0, 0.5, 0.5) on the faces, forming corner-sharing PBa_6 and PX_6 octahedra. To ensure the lowest ground energy and highest structural stability, the equilibrium lattice constant was optimized to yield the most stable structure (Fig. 1). The specific values of the optimized structural properties are shown in Table 1, such as the unit cell volume (in Å^3), equilibrium lattice constant a_0 (in Å), and ground state energy (in eV), all obtained from the PBE functional. The data from this table can be used to see that as the size of the halide anion grows (F, Cl, Br, or I), the lattice constants also increase. This trend is in good agreement with the fact that I has a larger ionic radius than F. In addition, the ground-state energy of Ba_3PX_3 (X = F, Cl, Br, I) decreases with increasing anion size, indicating that Ba_3PI_3 has the most stable configuration among all the compositions investigated.

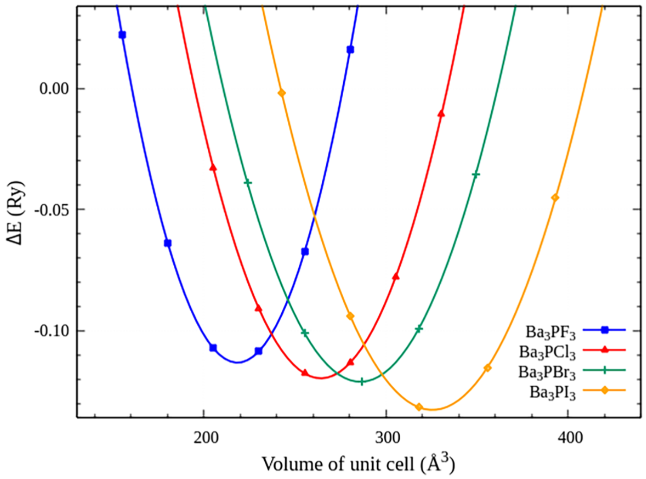

Figure 1: Volume-energy optimization curves for Ba_3PX_3 (X = F, Cl, Br, I) materials.

Table 1: Lattice constant (a_0), bulk modulus (B_0), first pressure derivative of bulk modulus (B_0'), and ground state energy (E_0) of the Ba_3PX_3 (X = F, Cl, Br, I).

Compounds	**a_0 (Å)**	**B (GPa)**	**B_0'**	**E_0 (eV)**
Ba_3PF_3	6.021, 5.90^a	31.985	3.589	−50,120.673
Ba_3PCl_3	6.415, 6.44^a, 6.47^c	28.574, 28.73^c	5.033, 4.46^c	−52,290.540
Ba_3PBr_3	6.586, 6.61^a	26.399	4.506	−65,161.319
Ba_3PI_3	6.869, 6.88^a, 6.76^b	23.166	4.661	−92,235.682

Note: ^{a}Reference [22]; ^{b}Reference [33]; ^{c}Reference [34].

The Bulk Modulus (B_0) quantifies resistance to hydrostatic compression and decreases from 31.985 GPa (Ba_3PF_3) to 23.166 GPa (Ba_3PI_3). These lower B_0 values illustrate the reverse trend of lattice expansion and indicate that as the atomic size of the halogen increases, the corresponding compounds become softer and more compressible. The observed decrease of B_0 points to a decrease in the average strength of inter-atomic bonding because the Ba–X and P–X bond lengths become longer in heavier halide systems. The positive First Pressure Derivative of Bulk Modulus (B_0') values illustrate that with the application of pressure, the materials under consideration will become less compressible, reflecting an increase in resistance to compression. This behaviour is consistent with the overall mechanical stability of the compounds. The Ground State Energy (E_0) values become more negative from −50,120.673 eV (Ba_3PF_3) to −92,235.682 eV (Ba_3PI_3), showing that there is a greater number of electrons and a greater total amount of binding energy for the heavier halide compound systems. The consistently negative values for the E_0 confirm the presence of thermodynamic stability for all of the investigated phase equilibrium points. The computed lattice parameters and their trend are in good agreement with the previously reported studies [22,33,34], which confirms the reliability of the adopted computational methodology.

3.2 Electronic Properties

To realize the electronic behaviour of the compositions considered and their uses in different areas, we calculated their electronic band structures using PBE functional along the high-symmetry directions R-Γ-X-M-Γ, with the Fermi level (E_F) set to 0 eV in the Brillouin zone. The calculated band-gap values obtained using the PBE functional, as shown in Table 2, are in good agreement with previously reported theoretical results [22,33,35], with minor variations arise from differences in computational parameters, structural optimization conditions, and methodological choices across different studies. To address the problem of the consistent underestimation of the bandgap by the traditional PBE functional [26] and achieve more accurate electronic bandgap values, the modified Becke-Johnson (mBJ) potential was used. The modified badstructures have been plotted and presented in Fig. 2. These bandstructures clearly demonstrate that the VBM and CBM of all the compounds are at the Γ-point, indicating a direct relationship between the structure and bandgap. The calculated PBE+mBJ bandgaps (Table 2) show a systematic decrease from 2.373 eV (Ba_3PF_3) to 1.480 eV (Ba_3PI_3). As the halide changes from F to I, a reduction in the bandgap occurs because the covalent nature of the Ba-X and P-X bonds is more pronounced. It decreases the energy difference between VBM & CBM.

Table 2: Bandgap and effective mass of Ba_3PX_3 (X = F, Cl, Br, I) compounds.

Compound	**Bandgap (eV)**		**Effective Mass**	
	PBE	**PBE+mBJ**	m_e^*/m_0	m_h^*/m_0
Ba_3PF_3	1.184, 0.94^a, 0.655^b	2.373	0.686	0.956
Ba_3PCl_3	1.149, 0.997^b	2.038	0.561	0.785
Ba_3PBr_3	1.099, 0.954^b	1.843	0.634	0.698
Ba_3PI_3	0.932, 0.797^b, 0.842^c	1.480	0.587	0.896

Note: ^{a}Reference [35]; ^{b}Reference [22]; ^{c}Reference [33].

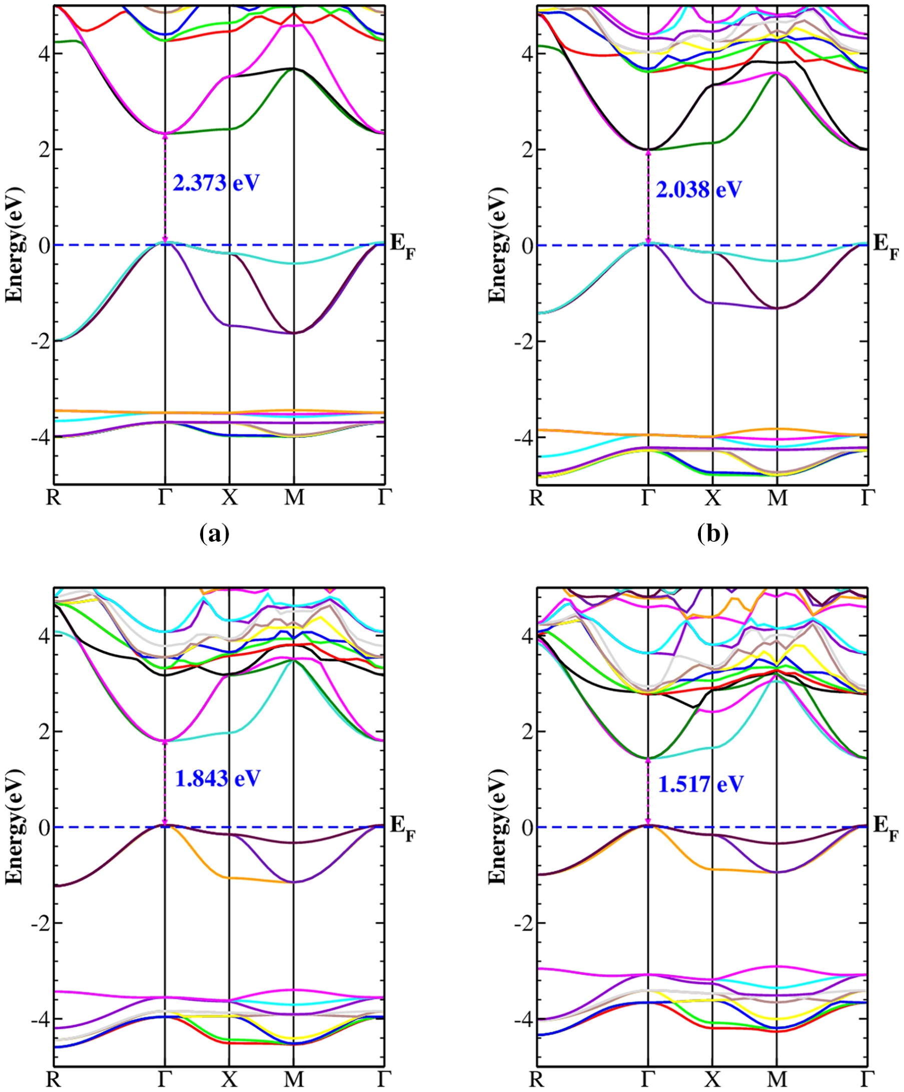

(a) (b)

(c) (d)

Figure 2: Bandstructure plot of (**a**) Ba_3PF_3, (**b**) Ba_3PCl_3, (**c**) Ba_3PBr_3, and (**d**) Ba_3PI_3.

The systematic decrease in the band gap from Ba_3PF_3 to Ba_3PI_3 can be explained by halide p-orbital energetics, electronegativity, and orbital overlap. The energy of the halide p orbitals decreased with a variation in the halogen from F to I because of the reduction in effective nuclear charge and principal quantum number. Simultaneously, the electronegativity of the halogen decreases, limiting the ionic nature of the P-X and Ba-X bonds and enhancing the covalent interaction. This decrease in electronegativity enhances the spatial overlap between the halide p and phosphorus p states, resulting in an increase in the maxima of the valence band. Consequently, the energy gap between the valence and conduction bands narrows as the series progresses. Additional evidence of the enlarged orbital overlap is that the bandwidth and dispersion are higher in the valence bands of Br- and I-based compounds, which confirms that halide substitution is a dominant factor in the electronic structure tuning of Ba_3PX_3 materials.

Fig. 3a–d shows the total and partial density of states (TDOS and PDOS) for the lead-free all-inorganic compounds Ba_3PF_3, Ba_3PCl_3, Ba_3PBr_3, and Ba_3PI_3, calculated via first-principles DFT. The DOS plots span an energy range of −5 to +5 eV with respect to the Fermi level (EF = 0 eV), highlighting the valence band and the conduction band. Each of these compounds has a clear forbidden band around the Fermi energy level, confirming their semiconducting nature. The valence band maxima are dominated by P-p states, with smaller participation from Ba-p/d and X-p states. This hybridization evolves systematically across the series, reflecting changes in P–X bonding character and halide p-orbital contributions. The evolution of hybridization is reflected in the band structures by the flattening of the valence bands for heavier halides, particularly in Ba_3PI_3. As the halogen atom changes from F to I, the crystal field and bonding environment around the Ba-P framework are modified, leading to a gradual upward shift of the Ba-P-dominated valence band edge, which is responsible for the progressive reduction of the band gap across the series. The CBM primarily arises from Ba-d states, with minor contributions from P-p orbitals. It indicates ionic Ba-X interactions and covalent P-X bonding, with the conduction band edge showing relatively similar dispersion across all four compounds, indicating that the conduction band position is only weakly affected by halogen substitution. The dominance of Ba-d orbitals near the CBM also accounts for the comparatively strong dispersion of the conduction bands, suggesting relatively moderate electron effective masses.

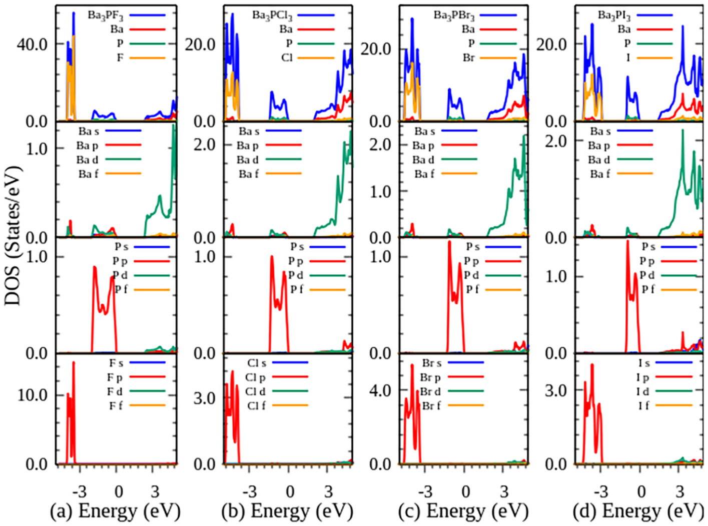

Figure 3: Total and partial DoS plots of (**a**) Ba_3PF_3, (**b**) Ba_3PCl_3, (**c**) Ba_3PBr_3, and (**d**) Ba_3PI_3.

As a measure of carrier transport, the effective masses of the electrons (m_e^*) and holes (m_h^*) were determined at the Γ-point and are provided in Table 2. For the studied materials, the electron effective mass lies in the range 0.561–0.686 m_0 and hole effective mass in the range 0.698–0.956 m_0. The non-monotonic variation is a result of the interplay between halide orbital and band hybridization. The effective mass of electrons is relatively low in the case of Ba_3PCl_3 and Ba_3PI_3, which implies that these elements have good electron transport, whereas Ba_3PBr_3 exhibits comparatively lower hole effective mass, suggesting improved hole mobility. Generally, m_h^* is greater than m_e^* of all compounds, and this means that they transport electrons more efficiently. These moderate values of effective mass justify the prospective application of Ba_3PX_3 compounds in optoelectronic and photovoltaic processes.

3.3 Optical Properties

This section provides a thorough analysis of the various optical characteristics of Ba_3PX_3, such as dielectric function, absorption spectra, optical conductivity, energy-loss function, reflectivity & refractive index over an energy range of 0–13 eV. The aim is to understand how these compounds behave when exposed to solar or other high energy sources. Information contained in optical spectra can be utilized to extract information about the induced polarization capacity and internal structure of the materials. For example, their bond types and band structure, as well as empty states can all be determined from an analysis of the material's optical spectra [36]. All optical properties were computed using the electronic structure obtained through the TB-mBJ potential to make them consistent with the better band-gap determination.

A material's optical properties can be described using the complex dielectric function, which is defined as [37]:

$$\varepsilon(\omega) = \varepsilon_1(\omega) + i\varepsilon_2(\omega) \tag{1}$$

where, ω is the angular frequency of the electromagnetic (EM) radiation incident on the material. The real part of the complex dielectric function, $\varepsilon_1(\omega)$, describes electronic polarization & anomalous dispersion, and the imaginary part, $\varepsilon_2(\omega)$, describes the optical absorption of the compounds. The imaginary part of the complex dielectric function, $\varepsilon_2(\omega)$, can be expressed in terms of $\varepsilon_1(\omega)$ [37]:

$$\varepsilon_2(\omega) = \frac{4e^2\pi^2}{\omega^2 m^2}\sum_{i,j}\int |\langle i|M|j\rangle|^2 f_i(1-f_i)\, X\delta\left(E_f - E_i - \hbar\omega\right) d^3k \tag{2}$$

here, the dipole matrix is represented by the symbol M, where i and j denote the initial state (valence band) and the final state (conduction band). The function f_i is the Fermi distribution function associated with the valence band. The expression $\delta(E_f - E_i - \hbar\omega)$ indicates the energy difference between the valence band and conduction band at a specific k point due to the absorption of a photon with an energy of $\hbar\omega$. The other variables are as follows: e = electron charge, ω = angular frequency of the photon, ħ = reduced Planck's constant (where $\hbar = h/2\pi$), and m = electron mass. To calculate $\varepsilon_1(\omega)$, the Kramers-Kronig transformation is used [37], as given below:

$$\varepsilon_1(\omega) = 1 + \frac{2}{\pi}P\int_0^{\infty}\frac{\omega'\varepsilon_2(\omega')}{\omega'^2 - \omega^2}d\omega' \tag{3}$$

The letter P denotes the integral's principal value. To analyse how the compounds we are studying respond to incoming light, we have measured their dielectric function, denoted as $\varepsilon(\omega)$.

Fig. 4a,b correspondingly demonstrates the real and imaginary parts of the $\varepsilon(\omega)$ as a function of the incoming EM energy. The static value of the $\varepsilon_1(\omega)$, i.e., $\varepsilon_1(0)$, also called the dielectric constant for the given sample, occurs at the low-end of our measurements. From the measurements, it can be observed that the $\varepsilon_1(0)$ was measured to be 2.75, 3.18, 3.57, and 4.35, respectively, for Ba_3PF_3, Ba_3PCl_3, Ba_3PBr_3, and Ba_3PI_3, respectively. Therefore, we have observed that as we increase the atomic size of the element in the X-position, the dielectric constant values also increase. This behaviour arises from an increase in polarizability, which increases the involvement of the lattice to the overall polarization. In particular, Ba_3PI_3 exhibits the highest $\varepsilon_1(0)$, indicating strong polarizability and a high optical permittivity. The negative values of $\varepsilon_1(\omega)$ after 7.06 eV of the compounds in the ultraviolet (UV) region indicate a plasmonic or metallic-like response, where the induced polarization oscillates out of phase with the incident EM field. This behaviour suppresses light propagation and results in strong reflection, associated with plasma resonance and intense interband electronic transitions. Fig. 4b represents the computed threshold energy values of $\varepsilon_2(\omega)$ for Ba_3PX_3 (X = F, Cl, Br, and I). Ba_3PF_3 does not exhibit any sharp peak in $\varepsilon_2(\omega)$; its maximum value occurs at 5.26 eV, after which it decreases, followed by a secondary increase and subsequent decline after reaching another maximum at 9.08 eV. Whereas for Ba_3PCl_3, Ba_3PBr_3, and Ba_3PI_3, $\varepsilon_2(\omega)$ shows sharp peaks at 8.59, 7.74, and 6.73 eV, correspondingly. The main peak in $\varepsilon_2(\omega)$ occurs in 5.26–8.59 eV energy range, indicating strong interband optical transitions in this region. Among all compounds, Ba_3PI_3 exhibits the highest intensity peak in $\varepsilon_2(\omega)$, suggesting enhanced optical absorption in the near-UV region.

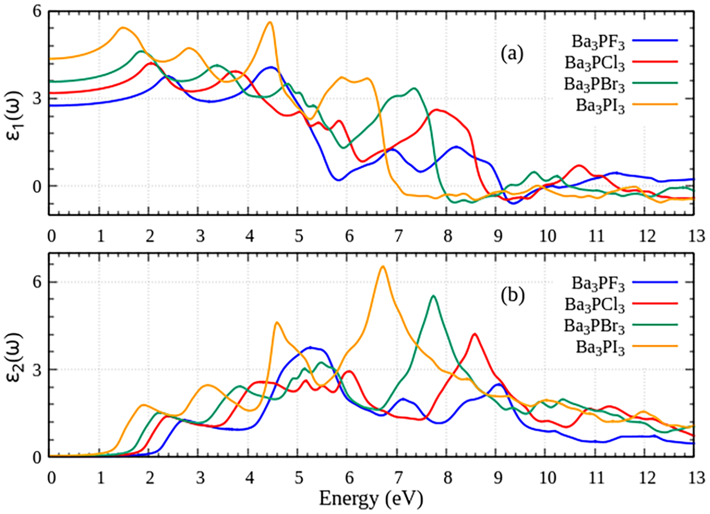

Figure 4: Variation in (**a**) $\varepsilon_1(\omega)$ and (**b**) $\varepsilon_2(\omega)$ of Ba_3PX_3 (X = F, Cl, Br, I) compositions with incident EM energy.

Fig. 5a presents curves for $\sigma(\omega)$, which represents the real part of optical conductivity for compositions studied. For all four compounds, $\sigma(\omega)$ has the highest values at energy of 9.08 eV for Ba_3PF_3, 8.59 eV for Ba_3PCl_3, 7.74 eV for Ba_3PBr_3, and 6.73 eV for Ba_3PI_3. As the anion changes from F to I, there is a general decrease in the corresponding energy value for peak values of $\sigma(\omega)$, indicating that the compounds have been further shifted towards lower photon energies. The pattern exhibited by $\sigma(\omega)$ is similar to that of the $\alpha(\omega)$ (Fig. 5b) and $\varepsilon_2(\omega)$ (Fig. 4b), indicating that Ba_3PI_3 and Ba_3PBr_3 have higher optical conductivity overall than Ba_3PF_3 and Ba_3PCl_3. Fig. 5b presents the optical absorption profiles of Ba_3PX_3 compounds. The absorption coefficient ($\alpha(\omega)$) defines the efficiency of light absorption, is a key parameter in evaluating solar energy conversion efficiency [38–40]. The value of $\alpha(\omega)$ was found to be the highest for Ba_3PBr_3 at 7.88 eV. After that, the peak value of $\alpha(\omega)$ for Ba_3PCl_3 and Ba_3PI_3 was observed as 8.78 eV and 6.84 eV, respectively. $\alpha(\omega)$ for Ba_3PF_3 was found to be the lowest compared to Ba_3PCl_3, Ba_3PBr_3, and Ba_3PI_3. The absorption peak of Ba_3PF_3 was found at 9.21 eV. The strong peaks in the $\varepsilon_2(\omega)$, $\sigma(\omega)$ and $\alpha(\omega)$ spectra are mainly due to interband transitions of the form P-p/X-p → Ba-d. The fact that these peaks shift to lower energies, for variation from Ba_3PF_3 to Ba_3PI_3, is in line with the gradually narrowing band gap and the increased P-p hybridization. The absorption edge of each compound is observed to be very similar to the values of the calculated direct band gap, which confirms the nature of direct transition in these materials. The systematic red-shift of the absorption edge of Ba_3PF_3 to Ba_3PI_3 is correlated with the decrease in band gap, and the heavier halide compositions absorb the visible light better. Increased polarizability and orbital overlap contribute to the increased intensity of optical peaks in Ba_3PI_3. These observations are consistent with previously reported halide perovskite systems, where band gap reduction, enhanced P-p/P-d hybridization, and increased polarizability with heavier halides lead to a systematic red-shift and stronger optical response [22,35].

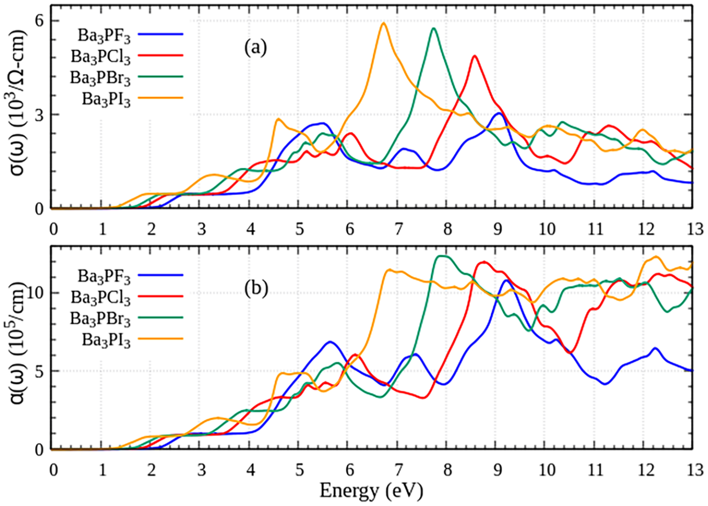

Figure 5: Variation in (**a**) σ(ω) and (**b**) α(ω) of Ba_3PX_3 (X = F, Cl, Br, I) compositions with incident EM energy.

Refractive index n(*ω*) and extinction coefficient k(ω) of Ba_3PX_3 compounds where X = F, Cl, Br and I are shown in Fig. 6a,b, respectively. The static value of n(ω) i.e., n(0), for Ba_3PX_3 compounds is 1.65, 1.78, 1.89 and 2.08, respectively, which increases with decreasing wavelength in the infrared and visible sections until it reaches a peak value of 2.09, 2.06, 2.15 and 2.47 at around 4.56, 2.08, 1.89 and 4.48 eV for Ba_3PF_3, Ba_3PCl_3, Ba_3PBr_3, and Ba_3PI_3, respectively. Following this point, the value of n(*ω*) continues to decrease; however, it will never be negative, which indicates that the compounds will still be transparent as the incident EM energy increases. Ba_3PI_3 had the highest value of n(0), which indicates that it will bend light more and allow for more potential applications with high refractive optical coatings. In Fig. 6b, the k(ω) value was found to be highest at 6.82 eV for Ba_3PI_3. The maximum k(ω) value was found to be at 7.85 eV for Ba_3PBr_3 and 8.69 eV for Ba_3PCl_3. The value of k(ω) for Ba_3PF_3 was found to be the lowest as compared to Ba_3PBr_3, Ba_3PCl_3, and Ba_3PI_3. The extinction coefficient peak of Ba_3PF_3 was found at 5.62 eV.

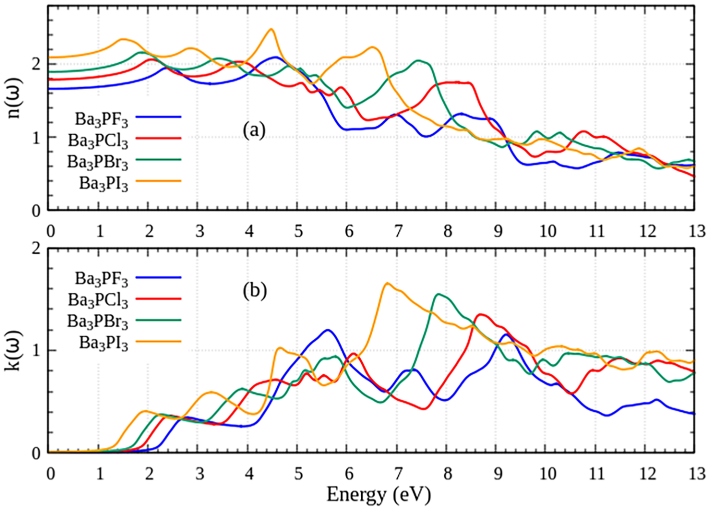

Figure 6: Variation in (**a**) n(ω) and (**b**) k(ω) of Ba_3PX_3 (X = F, Cl, Br, I) compositions with incident EM energy.

Reflectivity R(ω), which plays a crucial role in computing the reflected energy at interfaces, is presented in Fig. 7a. The zero-frequency reflectivity values are found to be 6.14% for Ba_3PF_3, 7.94% for Ba_3PCl_3, 9.48% for Ba_3PBr_3, and 12.40% for Ba_3PI_3. All compounds exhibit low reflectivity in the infrared and visible sections, demonstrating good transparency, while a noteworthy growth in reflectivity is found in the UV region, particularly for Ba_3PI_3, due to enhanced polarizability. In Fig. 7b, the peaks of the energy loss function $E_{loss}(\omega)$ for cubic Ba_3PX_3 structures are found in between 10–13 eV energy. These pronounced peaks correspond to plasma resonance arising from the collective oscillations of valence electrons, confirming the plasmonic behaviour of the materials in the UV region. $E_{loss}(\omega)$ defines the energy dissipated by fast electrons passing through the compound, rather than by direct interband transitions. The onset values of the dielectric constant, reflectivity, and refractive index for all the studied compounds have been mentioned in Table 3.

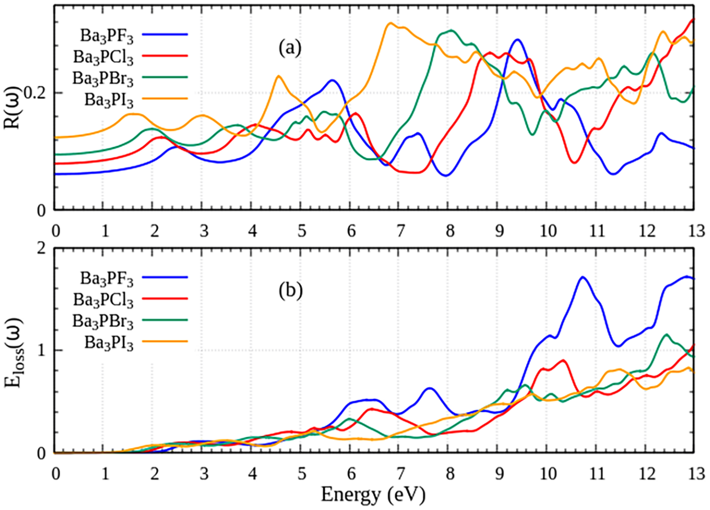

Figure 7: Variation in (**a**) R(ω) and (**b**) $E_{loss}(\omega)$ of Ba_3PX_3 (X = F, Cl, Br, I) compositions with incident EM energy.

Table 3: Optical characteristics of Ba_3PX_3 (X = F, Cl, Br, I) compositions.

Materials	**$\varepsilon_1(0)$**	**R(0) (%)**	**n(0)**
Ba_3PF_3	2.75, 6.78[a], 5.17[b]	6.14	1.65
Ba_3PCl_3	3.18, 5.02[a]	7.94	1.78
Ba_3PBr_3	3.57, 5.18[a]	9.48	1.89
Ba_3PI_3	4.35, 5.57[a]	12.40	2.08

Note: [a]Reference [22]; [b]Reference [35].

While the optical spectra of Ba_3PX_3 compounds are presented over a broad energy range extending into the UV region to capture all possible interband transitions, their photovoltaic relevance is primarily associated with the visible region of the spectrum (≈1.6–3.2 eV). In contrast, spectral features in the higher-energy UV region (>3.2 eV) arise from deeper interband transitions and are less relevant for solar energy harvesting. In the visible region, Ba_3PBr_3 and Ba_3PI_3 exhibit comparatively stronger absorption coefficients and higher dielectric response, indicating efficient photon harvesting within the solar spectral range. The relatively low reflectivity and moderate refractive indices further suggest favorable light coupling and reduced optical losses, which are advantageous for thin-film photovoltaic architectures where the absorber thickness is limited. Owing to their direct bandgap nature and strong visible-light absorption, efficient charge generation can be achieved at sub-micrometer thicknesses. Additionally, all optical properties reported here correspond to the isotropic response of the cubic crystal structure, as expected for the Pm-3m symmetry, and therefore do not exhibit directional anisotropy. This isotropic optical behavior is beneficial for device fabrication, as it ensures uniform light absorption irrespective of crystal orientation.

It should be noted that the current optical computations are based on the independent-particle DFT approach and do not include excitonic effects arising from electron–hole interactions. In practical substances, these effects may cause some small changes in the absorption onset and peak intensities, especially around the band edge. However, to perform comparative analysis across the Ba_3PX_3 series, the present method provides reliable trends in optical response. Similar approaches relating electronic structure to optical transitions have been reported in recent studies on semiconductor materials [41].

3.4 Theoretical Power Conversion Efficiency

It is important to estimate the theoretical efficiency of a material prior to screening it for photovoltaic absorber applications. Absorber thickness, intrinsic defects, carrier recombination dynamics, temperature, and optical absorption characteristics strongly govern the efficiency of a photovoltaic device. A single-junction solar cell is reflected by the Spectroscopic Limited Maximum Efficiency (SLME) [30] as a complete and trustworthy indicator that assesses the upper-limit efficiency of both the absorber and the solar cell, including realistic absorption spectra and bandgap characteristics of the absorber. It follows that the values of SLME should be treated as theoretical screening limits rather than practically achievable device efficiencies, because they do not account for non-radiative recombination, defects, and interface losses. The SLME framework assumes radiative recombination as the dominant recombination mechanism, representing an upper theoretical limit for photovoltaic efficiency.

We have shown the SLME as a function of the absorber layer thickness of the studied Ba_3PX_3 (X = F, Cl, Br, I) compositions at 300 K in Fig. 8a. It is evident from the plot that the SLME rises rapidly as the film thickness increases within the sub-micrometer range, then reaches a saturation limit at thicker films. In particular, Ba_3PF_3 has the lowest efficiency of 2.43% at very thin layers, 17.73% at close to 1 μm, and then stabilizes. This thickness (~1 μm) is representative of typical thin-film photovoltaic absorbers and is therefore considered a practical reference for efficiency evaluation. Ba_3PCl_3 and Ba_3PBr_3, however, have a higher rate of 25.86% and 30.97%, respectively. The maximum performance is observed in Ba_3PI_3, where SLME rises sharply and stabilizes at 39.17%. This tendency shows that the replacement of the halides with heavier anions increases optical absorption and the theoretical efficiency that can be achieved. Unlike idealized models, the SLME formalism incorporates the calculated absorption coefficient, thereby accounting for realistic absorption losses. The variation in SLME across the Ba_3PX_3 series is therefore directly influenced by the computed absorption spectra, with higher absorption coefficients in Ba_3PBr_3 and Ba_3PI_3 contributing to their enhanced efficiency. The saturation behaviour at thickness above 1 μm indicates that an additional increase in thickness is not significantly helpful in increasing photon absorption, as the optical path length is already long.

Fig. 8b plots the temperature dependence of the SLME for the same compounds, with a 1 μm constant thickness of absorber. The decrease in the SLME with rising temperature from 300 to 900 K across all compositions is evident and shows that photovoltaic performance is highly sensitive to temperature. In the case of Ba_3PF_3, the efficiency decreases to 17.73% at 300 K and 8.95% at 900 K. Likewise, it decreases to 11.97% and 13.39% for Ba_3PCl_3 and Ba_3PBr_3, respectively. The strongest decrease is seen in the case of Ba_3PI_3, with the SLME at 300 K being 39.17%, followed by 14.57% at 900 K. This decrease may be explained by increased carrier recombination and by the thermally induced narrowing of the bandgap at high temperatures.

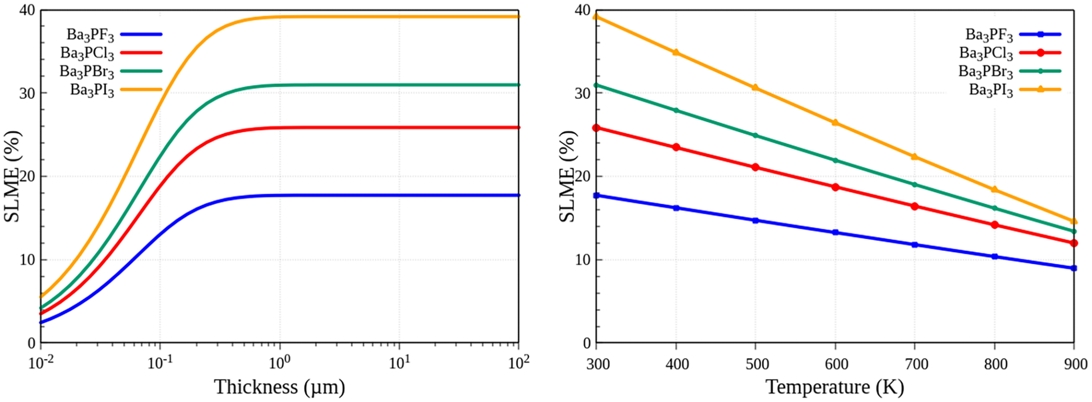

(a) **(b)**

Figure 8: (**a**) SLME as a function of absorption layer thickness at 300 K, and (**b**) SLME as a function of temperature for optimal thickness of absorption layer.

Ba_3PI_3 is the most efficient according to theory, though it is also relatively more sensitive to temperature changes than the other compounds being studied. It is worth noting that SOC, particularly relevant for Ba_3PI_3, may decrease the band gap and shift the onset of absorption, which could lead to a minor overestimation of the calculated values of the SLME. The total enhancement of SLME of F- to I-based compounds is indicative of the fact that the quality of absorber and optical response is enhanced with the heavier halide substitution. The materials are promising photovoltaic absorbers at the materials-screening level due to their relatively high values of SLME, especially in the case of Ba_3PBr_3 and Ba_3PI_3.

3.5 Elastic Properties

The systematic investigation of the elastic characteristics of Ba_3PX_3 (X = F, Cl, Br, I) compositions is done to realize their mechanical stability, bonding properties, anisotropy in elasticity, and ductile properties. The computed elastic parameters have been listed in Tables 4 and 5. Elastic constants in a single crystal and the mechanical parameters derived were obtained. These parameters define how the material responds to the external pressure and give an idea of the bonding nature of the material, directional anisotropic nature, and ductile nature. A cubic crystal is considered to be stable to elastic deformations when $C_{11} - C_{12} > 0$; $C_{44} > 0$; $C_{11} + 2C_{12} > 0$ and $C_{11} > 0$ [42]. Here, one defines Cauchy pressure as $C'' = C_{12} - C_{44}$. When the value is positive, this is a ductile behavior and when it is negative, this is a brittle behaviour [43]. Elastic constants, especially, C_{11}, C_{12}, and C_{44} are important to explain how a crystal reacts to external forces. The elastic constants of the Ba_3PX_3 family show non-monotonic variation based on competing influences from lattice expansion, bond strengths and hybridization of orbitals. As the halides increase in ionic radius, interatomic interaction is weakened; however, the character of P-X bonds and their associated local structural environments cause a non-linear response of these bonds to elastic deformations. C_{11} is usually the largest of the elastic constants, and is associated with longitudinal strain response in the primary crystallographic directions, whereas C_{12} and C_{44} are associated with compressive and shear effects, respectively. Even though C_{11} reaches its maximum with Ba_3PF_3 and its minimum with Ba_3PI_3, its change across the Ba_3PX_3 series is not monotonic. C_{11} and C_{44} vary non-monotonically, whereas C_{12} varies monotonically within the Ba_3PX_3 series; that is, the resistance increases monotonically with the increasing size of the halogen atom. The obtained values satisfy the Born stability criteria, indicating that the considered compositions are mechanically stable. The convergence of the elastic constants was validated by carefully controlling for computational parameters, while the optimized structures represent the stable energy minima; therefore, the trends are intrinsic and not a result of numerical artifacts.

Table 4: Calculated elastic constants (C_{11}, C_{12} and C_{44} in GPa); bulk Modulus (B in GPa); shear modulus (G in GPa); B/G Ratio; tetragonal shear modulus (C′); Cauchy's pressure (C″); Poisson's ratio (η), and Young's modulus (Y in GPa) of Ba_3PX_3 (X = F, Cl, Br, I) at ambient conditions.

Compound	C_{11}	C_{12}	C_{44}	B	G	B/G	C′	C″	η	Y
Ba_3PF_3	70.25, 54.10^a, 73.89^b	12.70, 1.87^a, 12.84^b	12.19, 15.67^a, 15.40^b	31.89, 19.28^a, 33.19^b	17.34, 19.25^a, 20.33^b	1.84, 1.00^a, 1.63^b	28.77	0.51	0.27, 0.12^a, 0.25^b	44.03, 43.34^a, 50.64^b
Ba_3PCl_3	63.60, 64.11^a, 70.37^c	10.94, 9.56^a, 10.34^c	17.29, 11.64^a, 10.97^c	28.49, 27.74^a	20.47, 16.50^a	1.39, 1.68^a, 1.82^c	26.33	−6.35, −0.6^c	0.21, 0.25^a, 0.27^c	49.55, 41.30^a
Ba_3PBr_3	65.24, 61.28^a	6.98, 8.87^a	13.07, 10.38^a	26.40, 26.34^a	18.13, 15.20^a	1.46, 1.73^a	29.13	−6.09	0.22, 0.26^a	44.25, 38.24^a
Ba_3PI_3	58.85, 55.03^a	5.60, 7.04^a	3.74, 8.27^a	23.35, 23.03^a	9.30, 12.89^a	2.51, 1.79^a	26.62	1.86	0.32, 0.26^a	24.62, 32.59^a

Note: [a]Reference [22]; [b]Reference [35]; [c]Reference [34].

Table 5: Computed Zener anisotropic index (A_Z); Kleinman parameter (ζ); Lame's coefficients (λ and μ); longitudinal, transverse, average sound velocities (v_l, v_t, and v_m in m/s) and Debye temperature (θ_D in K) of Ba_3PX_3 (X = F, Cl, Br, I) materials at ambient conditions.

Compound	A_Z	ζ	λ	μ	v_l	v_t	v_m	θ_D
Ba_3PF_3	0.42	0.33	20.33	17.34	3802.80	2134.94	2375.80	253.06
Ba_3PCl_3	0.66	0.32, 0.32^a	14.84	20.47	4018.50	2434.29	2690.37	268.96
Ba_3PBr_3	0.45	0.26	14.31	18.13	3569.88	2137.42	2364.98	230.29
Ba_3PI_3	0.14	0.24	17.15	9.30	2910.21	1484.06	1662.86	155.26

Note: [a]Reference [34].

The elastic parameters of a given material can be used to compute the bulk modulus (B) and shear modulus (G) of that material using the Voigt, Reuss, and Hill (VRH) approximation. In the case of a cubic structure, the bulk modulus computed by the Voigt approximation and the shear modulus computed by the Reuss approximation are the following [44,45].

$$B_V = B_R = \left(\frac{C_{11} + 2C_{12}}{3}\right) \tag{4}$$

$$G_V = \left(\frac{C_{11} - C_{12} + 3C_{44}}{5}\right) \tag{5}$$

$$G_R = \frac{5\left(C_{11} - C_{12}\right)C_{44}}{4C_{44} + 3\left(C_{11} - C_{12}\right)} \tag{6}$$

The actual values of the moduli, according to Hill [46], are calculated by the arithmetical mean of two separate moduli computed using the Voigt and Reuss approximations:

$$B = \left(\frac{B_V + B_R}{2}\right) \tag{7}$$

And

$$G = \left(\frac{G_V + G_R}{2}\right) \tag{8}$$

The bulk modulus (B) indicates the resistance of a specimen to uniform compression, while the shear modulus (G) indicates its stiffness against shear deformation. In the Ba_3PX_3 series, the values of these two moduli decreased from Ba_3PF_3 (B = 31.89 GPa, G = 17.34 GPa) to Ba_3PI_3 (B = 23.35 GPa, G = 9.3 GPa). This decrease indicates that the presence of heavy halide ions decreases the internal bond strength of the compounds, making them relatively more flexible. Therefore, Ba_3PF_3 was found to be the most rigid, and Ba_3PI_3 was found to be the most flexible. The brittleness or ductility of a substance can be judged by Pugh's ratio (B/G). If this ratio is greater than 1.75, the material is considered ductile, otherwise brittle. This ratio was found to be greater than 1.75 for Ba_3PF_3 and Ba_3PI_3, indicating their ductile nature. In contrast, Ba_3PCl3 and Ba_3PBr_3 had values below 1.75, making them moderately brittle, consistent with previous calculations [47].

Shear constant (C′) and Cauchy Pressure (C'') can be calculated as follows [48]:

$$C' = \left(\frac{C_{11} - C_{12}}{2}\right) \tag{9}$$

$$C'' = C_{12} - C_{44} \tag{10}$$

Analysis of Cauchy pressure (C'') also gives the same conclusion that while its positive value shows ductility, a negative value shows brittleness. Positive values were obtained for Ba_3PF_3 (0.51 GPa) and Ba_3PI_3 (1.86 GPa), which confirm their ductility. On the other hand, negative values for Ba_3PCl_3 and Ba_3PBr_3 were found to be −6.35 and −6.09 GPa, respectively, which makes them brittle in nature.

The Poisson's ratio (η) also remained within a stable range for all compounds, indicating mechanical stability and a predominantly ionic bonding character. Young's modulus (Y) is a fundamental indicator of a material's stiffness, representing its response to longitudinal strain. A higher value of Y corresponds to greater stiffness of the material. It can be calculated using the relation:

$$Y = \frac{9BG}{3B + G} \tag{11}$$

For the Ba_3PX_3 (X = F, Cl, Br, I) compositions, the Young's modulus varies from 24.62 GPa for Ba_3PI_3 to 49.55 GPa for Ba_3PCl_3, which indicates that Ba_3PCl_3 possesses higher stiffness, while Ba_3PI_3 exhibits greater elasticity. Additionally, values such as the Zener ratio (A_z) and the Kleinman parameter (ζ) were used to understand the isotropy and bonding behaviour of the compounds. A substance is considered isotropic when the Zener ratio is close to 1. As shown in Table 5, all compounds exhibit elastic anisotropy ($A_Z \neq 1$), with the degree of anisotropy varying non-monotonically across the halide series. With an anisotropy value nearest to unity ($A_Z = 0.66$), Ba_3PCl_3 has a relatively more isotropic mechanical behavior, which is advantageous to the homogeneous distribution of strain and minimized formation of defects in thin-film devices. Ba_3PI_3 ($A_Z = 0.14$) on the other hand exhibits the greatest level of anisotropy, which implies a stronger directional-dependent mechanical behavior that could affect the distribution of stress in the film growth. The rest of the compounds are moderately anisotropic indicating a balanced mechanical response that is appropriate to prepare a device.

The first Lamé constant (λ) is related to the degree of material compressibility, while the second Lamé constant (μ) is indicative of the degree of shear stiffness in a particular material. These coefficients can be defined by the following expressions using the Young's modulus and the Poisson's ratio of the considered compositions:

$$\lambda = \frac{Y\eta}{(1+\eta)(1-2\eta)} \tag{12}$$

$$\mu = \frac{Y}{2(1+\eta)} \tag{13}$$

Table 5 reports the calculated values of λ and μ for each of the investigated compositions. Only positive values of λ and μ exist for all compounds, as presented in Table 5. The positive value of λ and μ for each composition indicates that they possess mechanical stability, while variations in μ reflect differences in shear resistance across the Ba_3PX_3 series.

The Debye temperature (θ_D) is a key thermal property that is correlated to many different physical properties of a material, including the melting point and specific heat of the materials. The θ_D can be expressed as [49]:

$$\theta_D = \frac{h}{k}\left[\left(\frac{3n}{4\pi}\right)\left(\frac{N_A\rho}{M}\right)\right]^{1/3} v_m \tag{14}$$

where, v_m is the average sound velocity, h is Planck's constant, k is Boltzmann's constant, n is the number of atoms in unit cell of a compound, N_A is Avogadro's number, ρ is compound density, and M is molecular weight of a compound. In general, the higher the value of v_m or θ_D, the greater the strength of the bond. In polycrystalline materials, the average sound velocity, v_m, is defined by [50]:

$$v_m = \left[\frac{1}{3}\left(\frac{2}{v_t^3} + \frac{1}{v_l^3}\right)\right]^{-1/3} \tag{15}$$

where v_t and v_l are transverse and longitudinal sound velocities, which can be defined by means of elastic constants (B and G) using Navier's equation, as below:

$$v_t = \sqrt{\frac{G}{\rho}} \tag{16}$$

$$v_l = \sqrt{\frac{3B + 4G}{3\rho}} \tag{17}$$

The Debye temperature (θ_D), derived from average sound velocities, decreases systematically across the halide series, from 253.06 K (Ba_3PF_3) to 155.26 K (Ba_3PI_3). Such a decrease is an indication of weaker interatomic forces and higher atomic masses in the iodide member, which results in lower-lattice vibration frequencies. Altogether, the mechanical study proves that the Ba_3PX_3 compounds are elastically stable, with tuneable stiffness and ductility based on the halide component. The non-linear change in elastic parameters is observed to emphasize how halide substitution alters bond lengths, elastic anisotropy, and lattice dynamics in a complex manner.

The computed elastic properties indicate that Ba_3PX_3 have mechanical properties that are compatible with thin-film photovoltaic fabrication. The medium bulk and shear moduli indicate that it is mechanically sound enough to resist thermal cycling and residual stress in the deposits related to sputtering or evaporation operations or solution-based film growth. Specifically, the comparatively reduced stiffness and increased ductility of Ba_3PI_3 suggest improved strain resistance, which is desirable for reducing crack formation and delamination in flexible or large area devices. On the other hand, the increased rigidity of Ba_3PF_3 and Ba_3PCl_3 can be advantageous when structural stability and integrity are required. The flexibility-rigidity trade-off created by substituting halides offers a convenient design parameter to customize Ba_3PX_3 absorbers for desired photovoltaic and optoelectronic device architectures.

The determined elastic constants and mechanical parameters are reasonably consistent with previously determined values [22,34,35]. Minor discrepancies come as a result of the difference in the computational methods such as exchange-correlation functionals, k-point density, and structural optimization procedures. Notably, the uniform patterns that were identified throughout the Ba_3PX_3 series confirms the strength and stability of the current set of computations.

3.6 Thermodynamic Propertiesunder Temperature and Pressure

Using the Gibbs2 program [29], the thermodynamic parameters of the investigated compositions have been calculated. The thermodynamic properties were calculated for each of these compounds from 0 to 900 K, and the pressure effect calculations were done for the range 0–10 GPa based on the Quasiharmonic model. This approach accounts for volume-dependent phonon contributions on thermodynamic behavior and is widely used for studying temperature- and pressure-dependent properties of crystalline materials. Therefore, the obtained results provide reasonable representations of the thermal response and stability trends of the Ba_3PX_3 compounds over a broad temperature range. At higher temperatures, particularly for softer compounds such as Ba_3PI_3, minor deviations may arise due to increased anharmonic phonon interactions; however, the overall trends remain well described within the quasi-harmonic framework. The thermodynamic behaviour of Ba_3PX_3 (X = F, Cl, Br, I) at varying temperatures and pressures is illustrated in Figs. 9 and 10, which include the bulk modulus (B), the acoustic Debye temperature Θ_D, the coefficient of thermal expansion (α), the entropy (S), the specific heat at constant pressure (C_p), and the specific heat at constant volume (C_v). The bulk modulus (Fig. 9a–d) shows a monotonic change downward with temperature of all the compounds, and this implies that the lattice is softening as a result of progressive anharmonic vibrations of the atoms. Conversely, the applied pressure has a substantial positive effect on B, which indicates greater resistance to volume compression due to shorter interatomic distances. It is evident that there is a halogen-dependent trend with the stiffest being Ba_3PF_3 and the softest being Ba_3PI_3, as the ionic radius increases and the strength of PX bonds between F and I weaken. The same applies to the Θ_D (Fig. 9e–h), which declines with temperature since the phonons become soft, and also rises with pressure since phonons become hard. The progressively reduced Θ_D values of heavier halogens are another indication that the predominant factors controlling lattice vibrations are atomic mass and bond strength. The thermal expansion coefficient (Fig. 9i–l) shows a rapid increase at low temperatures and a slow increase at high temperatures, which is a characteristic feature of anharmonic lattice dynamics. The pressure is inhibitory to α in any system, with lattice compression limiting the anharmonic atomic mobility. The larger alpha values of Ba_3PBr_3 and Ba_3PI_3 are explained by their lower bulk moduli and acoustic Debye temperatures, indicating greater lattice flexibility.

All compositions and pressures show a monotonically increasing entropy (Fig. 10a–d) as the temperature increases, which is evidence of the gradual filling up of phonon modes. Entropy decreases with pressure at a specified temperature; compression decreases the available vibrational phase space. The more massive systems have greater entropy, due to both lower characteristic phonon frequencies and a stronger vibrational disorder. Both C_v (Fig. 10e–h) and C_p (Fig. 10i–l) increase steeply at low temperatures and tend towards saturation at high temperatures, as observed in Debye theory. At higher temperatures, C_v approaches the

Dulong-Petit limit, verifying the classical vibrational behaviour of the lattice. That minor surplus of C_p over C_v rises with temperature and falls with pressure, and, in harmony with thermodynamic relations between heat capacity and thermal expansion, is negative. In this way, the calculated thermodynamic parameters reveal a strong interdependence among mechanical stiffness, lattice vibrations, and thermal response in Ba_3PX_3 compounds. The lattice is stabilized by pressure, which improves stiffness, raises Θ_D, and inhibits thermal expansion and entropy. The substitution of a halogen by a suitable element is found to be a viable path to achieving thermodynamic softness and tuning vibrational behaviour. This tunability is highly valuable when thermal and mechanical stability are required across different operating conditions.

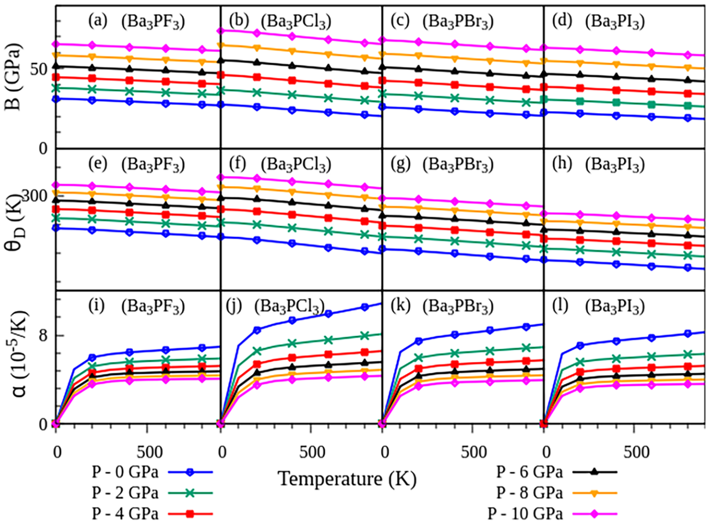

Figure 9: Temperature dependence of the (**a**–**d**) bulk modulus (B), (**e**–**h**) acoustic Debye temperature (Θ_D), and (**i**–**l**) linear thermal expansion coefficient (α) for (**a**,**e**,**i**) Ba_3PF_3, (**b**,**f**,**j**) Ba_3PCl_3, (**c**,**g**,**k**) Ba_3PBr_3, and (**d**,**h**,**l**) Ba_3PI_3 under pressures ranging from 0 to 10 GPa.

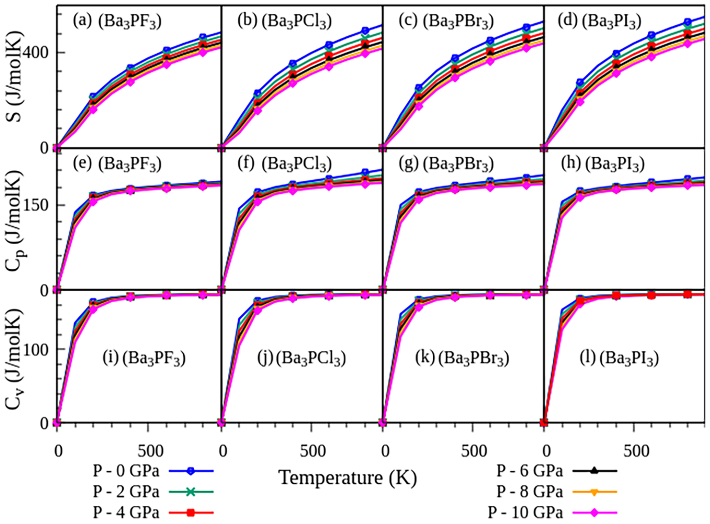

Figure 10: Temperature-dependent (**a**–**d**) entropy (S), (**e**–**h**) specific heat at constant pressure (C_p), and (**i**–**l**) specific heat at constant volume (C_v) for (**a**,**e**,**i**) Ba_3PF_3, (**b**,**f**,**j**) Ba_3PCl_3, (**c**,**g**,**k**) Ba_3PBr_3, and (**d**,**h**,**l**) Ba_3PI_3 calculated under applied pressures up to 10 GPa.

The trend of the Grüneisen parameter (γ) that is used to gauge anharmonicity and phonon-volume coupling is $Ba_3PF_3 < Ba_3PI_3 < Ba_3PBr_3 < Ba_3PCl_3$. This observation (non-mass-monotonic) suggests that the atomic mass of halides, bonding properties, and lattice rigidity are reflected in the values of γ. The relatively higher γ values of Br-based and Cl-based compounds indicate more phonon volume coupling due to intermediate electronegativity and more flexible P-X bonds prevailing over mass-driven phonon softening. In terms of devices, the moderate values of γ (1.49–2.17) suggest that there is enough anharmonicity to allow thermal expansion and strain throughout the manner of operation, and the lattice is stable. Such a balance helps maintain the thermal stability of the Ba_3PX_3 material in photovoltaic applications under operating conditions. At 300 K, the computed thermodynamic parameters are represented in Table 6. The moderate values of γ also indicate that anharmonic effects remain within a manageable range, supporting the validity of the quasi-harmonic approximation over the studied temperature range, although minor deviations may arise at higher temperatures, particularly for softer compounds.

Table 6: Thermodynamic parameters of Ba_3PX_3 (X = F, Cl, Br, I) at 300 K.

Compound	B (GPa)	θ_D	α (10^{-5}/K)	S (J/mol-K)	C_v(J/mol-K)	C_p(J/mol-K)	γ
Ba_3PF_3	29.89	226.67	6.31	284.21	169.72	174.52	1.49
Ba_3PCl_3	25.16	203.80, 220.58[a]	8.98	302.31	170.64	180.62	2.17
Ba_3PBr_3	24.03	181.00	7.83	322.60	171.47	179.26	1.94
Ba_3PI_3	21.33	159.13	7.34	344.74	172.17	179.05	1.82

Note: [a] Reference [34].

The computed thermodynamic parameters also contain significant information about the functional behaviour of Ba_3PX_3 materials with respect to temperature. The reduction in B and θ_D with increasing temperature indicates lattice softening that can lead to bandgap renormalization and increased electron-phonon interactions. The increase in carrier recombination and thermally induced broadening of the bandgap is consistent with the observed reduction in SLME at elevated temperatures. An increase in entropy and heat capacity indicates an increase in phonon population; increased phonons can affect carrier scattering and optical absorption close to the band edge. Heavier halide materials were observed to have lower θ_D, which indicates that stronger vibrations within the lattice structure which can lead to greater temperature sensitivity in their electronic/optical responses.

4 Conclusion

This study establishes clear structure-property-performance relationships in the Ba_3PX_3 (X = F, Cl, Br, I) family and demonstrates the decisive role of halide substitution in governing their functional behaviour. The expansion of the lattice (6.02–6.87 Å) and softening of the crystal are reflected by a decrease in bulk modulus of 31.985 GPa (Ba_3PF_3) to 23.166 GPa (Ba_3PI_3) with the systematic increase in halide ionic size. The progressive narrowing of the bandgap, from 2.37 to 1.48 eV, associated with this mechanical softening, is due to greater polarizability and p-p hybridization. As a result, optical response increases significantly throughout the series as the dielectric constants increase from 2.75 to 4.35 and the refractive indices from 1.65 to 2.08, showing a stronger light-matter interaction in Br- and I-containing compounds. The trends are captured in the calculated photovoltaic screening performance, in which SLME increases sharply between Ba_3PF_3 and Ba_3PI_3 to 30.97% and 39.17%, respectively, at 300 K. The present analysis focuses on ideal bulk properties and provides a clear understanding of the intrinsic structure–property relationships in Ba_3PX_3 compounds. Incorporating additional effects such as spin–orbit coupling, defect states, and interface phenomena in future studies will further refine the assessment of their performance under practical device conditions, along with experimental validation.

Acknowledgement: The authors are thankful to the Centre for Research, Instrumentation & Development (CRID), Poornima University, Jaipur, for providing the necessary facilities.

Funding Statement: This work was supported by Poornima University, Jaipur, through a Seed Money Grant (Ref. No. PU/REG/2025-26/5283/1).

Author Contributions: The authors confirm contribution to the paper as follows: study conception and design: Peeyush Kumar Kamlesh, Himanshi Sharma; data collection: Shrikant Verma; analysis and interpretation of results: Peeyush Kumar Kamlesh, Ajay Singh Verma, Reena Saxena; draft manuscript preparation: Peeyush Kumar Kamlesh, Dinesh C. Sharma. All authors reviewed and approved the final version of the manuscript.

Availability of Data and Materials: The data that support the findings of this study are available from the corresponding author, Peeyush Kumar Kamlesh, upon reasonable request.

Ethics Approval: Not applicable

Conflicts of Interest: The authors declare no conflicts of interest.

References

1. Nawaz Romel MS, Mondal RN, Fatema-Tuz-Zahra, Islam MR, Gomha SM, Zaki MEA, et al. Theoretical and device-level insights into $FASnBr_3$ perovskite solar cells: a synergistic approach Combining density functional theory and SCAPS-1D. Results Phys. 2026;82(3):108593. doi:10.1016/j.rinp.2026.108593.
2. Rolania MC, Kamlesh PK, Kumar P, Sharma G, Verma AS. Insights into structural stability and thermal energy conversion into electrical properties of Mg_3X_2 (X = P, As, and Sb) compounds: a first-principles study. Mod Phys Lett B. 2025;39(22):2550081. doi:10.1142/s0217984925500812.
3. Manzoor M, Dixit A, Sharma R, Sardor S, Hayitov A, Ghodhbani R, et al. A computational investigation of novel perovskite halides $LiCrX_3$(X = Cl, Br) for spintronics and energy conversion applications. Mod Phys Lett B. 2026;40(4):2550270. doi:10.1142/s0217984925502707.
4. Meena A, Bairwa JK, Kumari S, Rani U, Kamlesh PK, Singh AP, et al. Structural, electronic and optoelectronic characteristics by first principles calculations for $CH_3NH_3PbBr_3$ hybrid perovskite. Phys Chem Solid State. 2025;26(1):10–22.
5. Luo D, Yang W, Wang Z, Sadhanala A, Hu Q, Su R, et al. Enhanced photovoltage for inverted planar heterojunction perovskite solar cells. Science. 2018;360(6396):1442–6. doi:10.1126/science.aap9282.
6. Bencherif H, Khalid Hossain M. Design and numerical investigation of efficient $(FAPbI_3)_{1-x}(CsSnI_3)_x$ perovskite solar cell with optimized performances. Sol Energy. 2022;248(23):137–48. doi:10.1016/j.solener.2022.11.012.
7. Schileo G, Grancini G. Lead or no lead? Availability, toxicity, sustainability and environmental impact of lead-free perovskite solar cells. J Mater Chem C. 2021;9(1):67–76. doi:10.1039/d0tc04552g.
8. Shi Z, Guo J, Chen Y, Li Q, Pan Y, Zhang H, et al. Lead-free organic-inorganic hybrid perovskites for photovoltaic applications: recent advances and perspectives. Adv Mater. 2017;29(16):1605005. doi:10.1002/adma.201605005.
9. Pandit N, Singh R, Joshi TK, Shukla A, Kamlesh PK, Dubey A, et al. Investigation of a potential photovoltaic absorber based on first principles spectroscopic screening of chalcogenide perovskites: $CaZrX_3$ (X = S, Se). J Comput Electron. 2024;24(1):11. doi:10.1007/s10825-024-02245-7.
10. Kumari S, Rani U, Rani M, Singh R, Kamlesh PK, Kumari S, et al. Computational investigation of the fundamental physical properties of lead-free halide double perovskite Rb_2NaCoX_6 (X = Cl, Br, and I) materials: potential prospects for sustainable energy. Mod Phys Lett B. 2024;38(34):2450323. doi:10.1142/s0217984924503238.

11. Chen G, Li N, Li W, Liu X, Ning T, Wang X, et al. Buried interface modification with nanoparticles for efficient perovskite solar cells with improved reproducibility. ACS Appl Energy Mater. 2025;8(11):6897–904. doi:10.1021/acsaem.5c01107.
12. Unger E, Jacobsson TJ. Tackling the reproducibility gap in perovskite research: a vision for FAIR data and standardised protocols. EES Sol. 2026;2(1):88–91. doi:10.1039/d5el00163c.
13. Sun K, Guo R, Zhou Q, Fang L, Jiang X, Wegener SA, et al. Insights into the operational stability of wide-bandgap perovskite and tandem solar cells under rapid thermal cycling. Nat Commun. 2026;17:596. doi:10.1038/s41467-025-68219-w.
14. Jiao B, Tan L, Ye Y, Ren N, Li M, Li H, et al. One-stone-two-birds: over 26% efficiency in perovskite solar cells via synergistic crystallization & interface regulation. Energy Environ Sci. 2025;18(11):5437–47. doi:10.1039/d5ee00189g.
15. Balagowtham N, Acchutharaman KR, Pandian MS, Kumar M, Chang JH, Ramasamy P. Challenges in commercializing perovskite solar cells with focus on sustainability, stability, and cost efficiency. Sol Energy. 2025;301(Suppl 1):113892. doi:10.1016/j.solener.2025.113892.
16. Parosh MBH, Saiduzzaman M, Islam J, Nisha NJ, Ovi IA. A first-principles study of dynamically stable non-toxic photovoltaic Mg_3PX_3 (X = Cl and Br) compounds. RSC Adv. 2025;15(13):10085–105. doi:10.1039/d5ra01185j.
17. Haque MM, Shimul AI, Ghosh A, Awwad NS, Chaudhry AR. Investigation of pressure-driven band gap variation and the physical characteristics of Ba_3SbX_3 (X = F, Cl) perovskite for potential optoelectronic applications. Opt Express. 2025;33(14):30486–504. doi:10.1364/OE.566477.
18. Green MA, Dunlop ED, Yoshita M, Kopidakis N, Bothe K, Siefer G, et al. Solar cell efficiency tables (version 67). Prog Photovolt. 2026;34(4):482–96. doi:10.1002/pip.70068.
19. Dey NL, Reza MS, Ghosh A, Al-Dmour H, Moumita M, Reza MS, et al. Optimization of $Sr3NCl_3$-based perovskite solar cell performance through the comparison of different electron and hole transport layers. J Phys Chem Solids. 2025;196:112386. doi:10.1016/j.jpcs.2024.112386.
20. Reza MS, Reza MS, Ghosh A, Rahman MF, Rajabathar JR, Ahmed F, et al. New highly efficient perovskite solar cell with power conversion efficiency of 31% based on Ca_3NI_3 and an effective charge transport layer. Opt Commun. 2024;561:130511. doi:10.1016/j.optcom.2024.130511.
21. Reza MS, Ghosh A, Gassoumi A, Hasan MR, Shahjalal M, Yahia AKM, et al. A comprehensive investigation involving numerous HTL and ETL layers to design and simulate high-efficiency Ca_3AsI_3-based perovskite solar cells. Inorg Chem Commun. 2025;172:113647. doi:10.1016/j.inoche.2024.113647.
22. Al Ijajul Islam M, Rahman MF, Islam MM, Mohammed MKA, Irfan A. Investigation of novel all-inorganic perovskites Ba_3PX_3 (X = F, Cl, Br, I) with efficiency above 29%. Phys Chem Chem Phys. 2025;27(4):1861–83. doi:10.1039/d4cp04276j.
23. Talukder MR, Hasan MM, Nayeem NM, Islam MR, Al-Humaidi JY, Islam MR, et al. Theoretical insights into novel Ba_3MX_3 (M = P, Sb; X = F, Cl) perovskites for advanced optoelectronics: a first-principles DFT study. Comput Theor Chem. 2025;1248:115239. doi:10.1016/j.comptc.2025.115239.
24. Blaha P, Schwarz K, Tran F, Laskowski R, Madsen GKH, Marks LD. WIEN2k: an APW+lo program for calculating the properties of solids. J Chem Phys. 2020;152(7):074101. doi:10.1063/1.5143061.
25. Perdew JP, Burke K, Ernzerhof M. Generalized gradient approximation made simple. Phys Rev Lett. 1996;77(18):3865–8. doi:10.1103/physrevlett.77.3865.
26. Tran F, Blaha P. Accurate band gaps of semiconductors and insulators with a semilocal exchange-correlation potential. Phys Rev Lett. 2009;102(22):226401. doi:10.1103/physrevlett.102.226401.
27. Zafar M, Muddassir M, Ali A, Shakil M, El Azab IH. Comparative analysis of band gap using different approximations, structural, mechanical and optical behaviour analysis of lead free double halide perovskites $Cs_2AgBiBr_6$ using DFT approach. Solid State Commun. 2025;397(9):115825. doi:10.1016/j.ssc.2024.115825.
28. Khan A, Khan NU, Ullah K, Iqbal J, Ullah H, Rehman A. DFT-based study of Na_2AgAlX_6 (X = Cl, Br) halide double perovskites: insights from PBEsol, TB-mBJ, and HSE06 calculations for photovoltaic and photocatalytic applications. Phys Scr. 2025;100(5):055946. doi:10.1088/1402-4896/adc846.

29. Otero-de-la-Roza A, Abbasi-Pérez D, Luaña V. Gibbs2: a new version of the quasiharmonic model code. II. Models for solid-state thermodynamics, features and implementation. Comput Phys Commun. 2011;182(10):2232–48. doi:10.1016/j.cpc.2011.05.009.
30. Yu L, Zunger A. Identification of potential photovoltaic absorbers based on first-principles spectroscopic screening of materials. Phys Rev Lett. 2012;108(6):068701. doi:10.1103/physrevlett.108.068701.
31. Sabino FP, Zhao XG, Dalpian GM, Zunger A. Impact of symmetry breaking and spin-orbit coupling on the band gap of halide perovskites. Phys Rev B. 2024;110(3):035160. doi:10.1103/physrevb.110.035160.
32. Gul B, Salman Khan M, Aasim M, Lfseisi AA, Khan G, Ahmad H. First-principles investigation of novel alkali-based lead-free halide perovskites for advanced optoelectronic applications. ACS Omega. 2023;8(36):32784–93. doi:10.1021/acsomega.3c03756.
33. Prasath LR, Selvakumar P. A comparative theoretical study of structural, electronic, and optical properties of A_3PI_3 (A = Ca, Ba, Mg) compounds for photovoltaic applications. Phys Solid State. 2025;67(7):548–55. doi:10.1134/s1063783425600335.
34. Rehman ZU, Lin Z. Inorganic M_3ACl_3 (M = Ca, Sr, Ba, A = N, P, As) perovskite-derivatives for next-generation solar cells and optoelectronics: in-depth analysis of stability, optoelectronic features, and temperature-dependent carrier mobilities. J Mater Chem A. 2025;13(40):34469–92. doi:10.1039/d5ta05368d.
35. Rabbi Talukder M, Mehedi Hasan M, Al-Humaidi JY, Quraishi AM, Rasidul Islam M, Masud Rana M. A DFT and AIMD study on the physical and optoelectronic properties of novel A_3PF_3 (A = Ca, Sr, and Ba) perovskites for energy harvesting applications. J Inorg Organomet Polym Mater. 2026;36(1):341–61. doi:10.1007/s10904-025-03922-1.
36. Dahbi S, Tahiri N, El Bounagui O, Ez-Zahraouy H. The new eco-friendly lead-free zirconate perovskites doped with chalcogens for solar cells: *ab initio* calculations. Opt Mater. 2020;109(2):110442. doi:10.1016/j.optmat.2020.110442.
37. Kamlesh PK, Gupta UK, Verma S, Rani M, Toual Y, Verma AS. *Ab initio* study of mechanical and functional properties of novel CaZnC and CaZnSi half-Heusler materials. Condens Matter Phys. 2025;28(4):43706. doi:10.5488/cmp.28.43706.
38. Ullah M, Ullah N, Tighezza AM, Bashir B, Batool K, Murtaza G. Bandgap nature transition and the optical properties of ABX_3 (A = K, Rb; B = Sr, Ba, Ca; X = Cl, Br, I) perovskites under pressure. J Inorg Organomet Polym Mater. 2025;35(1):552–69. doi:10.1007/s10904-024-03270-6.
39. Wang S, Huang M, Wu YN, Chen S. Absolute volume deformation potentials of inorganic ABX_3 halide perovskites: the chemical trends. Adv Theory Simul. 2021;4(6):2100060. doi:10.1002/adts.202100060.
40. Chaba Mouna S, Radjai M, Bouhemadou A, Rahman MA, Kara H, Houatis D, et al. Structural, electronic, and optical characteristics of $BaXCl_3$ (X = Li, Na) perovskites. Mater Sci Eng B. 2024;308:117578. doi:10.1016/j.mseb.2024.117578.
41. Nematov D. Analysis of the optical properties and electronic structure of semiconductors of the Cu_2NiXS_4 (X = Si, Ge, Sn) family as new promising materials for optoelectronic devices. J Opt Photonics Res. 2024;1(2):91–7. doi:10.47852/bonviewjopr42021819.
42. Karki BB, Stixrude L, Clark SJ, Warren MC, Ackland GJ, Crain J. Structure and elasticity of MgO at high pressure. Am Mineral. 1997;82(1–2):51–60. doi:10.2138/am-1997-1-207.
43. Harun-Or-Rashid M, Ben Farhat L, Brahmia A, Mohammed MKA, Rahman MA, Azzouz-Rached A, et al. Analysis of the role of A-cations in lead-free A_3SbI_3 (A = Ba, Sr, Ca) perovskite solar cells. J Mater Sci. 2024;59(15):6365–85. doi:10.1007/s10853-024-09579-4.
44. Voigt W. On the relation between the elasticity constants of isotropic bodies. Ann Phys Chem. 1889;274:573–87.
45. Reuss A. Berechnung der fließgrenze von mischkristallen auf grund der plastizitätsbedingung für einkristalle. Z Für Angew Math Und Mech. 1929;9(1):49–58. doi:10.1002/zamm.19290090104.
46. Hill R. The elastic behaviour of a crystalline aggregate. Proc Phys Soc A. 1952;65(5):349–54. doi:10.1088/0370-1298/65/5/307.

47. Habibpourbisafar R, Nemati F, Javanshoor E, Simserides C. Dual cation-anion substitution in phosphorus-based perovskites A_3PX_3 (A = Ca, Sr; X= Cl, F): structural, mechanical, electronic, and optical properties. J Phys Condens Matter. 2026;38(7):075701. doi:10.1088/1361-648X/ae430c.
48. Pokluda J, Černý M, Šob M, Umeno Y. *Ab initio* calculations of mechanical properties: methods and applications. Prog Mater Sci. 2015;73(Part A):127–58. doi:10.1016/j.pmatsci.2015.04.001.
49. Mahmood Q, Yaseen M, Hassan M, Rashid MS, Tlili I, Laref A. The first-principle study of mechanical, optoelectronic and thermoelectric properties of $CsGeBr_3$ and $CsSnBr_3$ perovskites. Mater Res Express. 2019;6(4):045901. doi:10.1088/2053-1591/aaf997.
50. Kuma S, Woldemariam MM. Structural, electronic, lattice dynamic, and elastic properties of $SnTiO_3$ and $PbTiO_3$ using density functional theory. Adv Condens Matter Phys. 2019;2019:3176148. doi:10.1155/2019/3176148.